

RADIATIVE TRANSFER SIMULATIONS FOR NEUTRON STAR MERGER EJECTA

MASAOMI TANAKA¹ AND KENTA HOTOKEZAKA²

Draft version September 30, 2018

ABSTRACT

The merger of binary neutron stars (NSs) is among the most promising gravitational wave (GW) sources. Next-generation GW detectors are expected to detect signals from the NS merger within 200 Mpc. Detection of electromagnetic wave (EM) counterpart is crucial to understand the nature of GW sources. Among possible EM emission from the NS merger, emission powered by radioactive r-process nuclei is one of the best targets for follow-up observations. However, prediction so far does not take into account detailed r-process element abundances in the ejecta. We perform radiative transfer simulations for the NS merger ejecta including all the r-process elements from Ga to U for the first time. We show that the opacity in the NS merger ejecta is about $\kappa = 10 \text{ cm}^2 \text{ g}^{-1}$, which is higher than that of Fe-rich Type Ia supernova ejecta by a factor of ~ 100 . As a result, the emission is fainter and longer than previously expected. The spectra are almost featureless due to the high expansion velocity and bound-bound transitions of many different r-process elements. We demonstrate that the emission is brighter for a higher mass ratio of two NSs and a softer equation of states adopted in the merger simulations. Because of the red color of the emission, follow-up observations in red optical and near-infrared (NIR) wavelengths will be the most efficient. At 200 Mpc, expected brightness of the emission is $i = 22\text{-}25$ AB mag, $z = 21\text{-}23$ AB mag, and 21-24 AB mag in NIR *JHK* bands. Thus, observations with wide-field 4m- and 8m-class optical telescopes and wide-field NIR space telescopes are necessary. We also argue that the emission powered by radioactive energy can be detected in the afterglow of nearby short gamma-ray bursts.

Subject headings: gamma-ray burst: general – gravitational waves – nuclear reactions, nucleosynthesis, abundances – radiative transfer – supernovae: general

1. INTRODUCTION

The merger of binary neutron stars (NSs) is among the most promising candidates for the direct detection of gravitational waves (GWs). Next-generation GW detectors, such as advanced LIGO, advanced VIRGO, and KAGRA (Abadie et al. 2010b; Kuroda & LCGT Collaboration 2010; Accadia et al. 2011; LIGO Scientific Collaboration et al. 2013), are expected to detect GWs from the NS merger at a distance within 200 Mpc. Statistical studies have shown that the number of GW detection will be in a range of 0.4-400 per year (Abadie et al. 2010a; Coward et al. 2012).

Follow-up observations of electromagnetic wave (EM) counterparts are essentially important. Only with the GW detection, the position of the sources can only be moderately determined with a localization of about 10-100 deg² (e.g., LIGO Scientific Collaboration et al. 2012, 2013; Nissanke et al. 2013). Therefore, to fully understand the nature of the GW sources, EM observations should pin down the position of the sources and identify the host galaxy and environment.

Possible EM emissions from the NS merger (e.g., Kochanek & Piran 1993; Metzger & Berger 2012; Rosswog et al. 2013; Piran et al. 2013) are (1) short gamma-ray bursts (GRBs), (2) radio/optical afterglow, and (3) emission powered by the radioactive decay energy. Among them, the last one is of great interest

because of the isotropic nature of the emission and a relatively short time delay after the merger (i.e., the detection of GWs).

By the merger of binary NSs, a small fraction of matter is expected to be ejected (e.g., Rosswog et al. 1999; Rosswog 2005; Lee & Ramirez-Ruiz 2007; Duez 2010; Goriely et al. 2011; Rosswog 2013; Hotokezaka et al. 2013; Bauswein et al. 2013). Hereafter we call this ejected material “NS merger ejecta”. NS merger ejecta is one of the promising sites for r-process nucleosynthesis (e.g., Lattimer & Schramm 1974, 1976; Eichler et al. 1989; Freiburghaus et al. 1999; Roberts et al. 2011; Goriely et al. 2011; Korobkin et al. 2012; Bauswein et al. 2013). Some of the synthesized r-process nuclei can provide radioactive decay energy with a timescale of 1-10 days or so. Li & Paczyński (1998) first proposed that this radioactive decay energy gives rise to the emission in the UV-optical-IR (UVOIR) wavelength range. This emission, which is similar to the emission of supernovae (SNe) powered by ⁵⁶Ni, has been called “macronova” (Kulkarni 2005), “kilonova” (Metzger et al. 2010; Metzger & Berger 2012), or “mini-SN”.

The brightness and the duration of the emission are mainly determined by (1) the mass and (2) the velocity of the ejecta, and also (3) opacity in the ejecta. Metzger et al. (2010) first presented detailed study of this emission by taking into account the radioactive energy based on the nucleosynthesis calculations. Roberts et al. (2011) and Goriely et al. (2011) also showed expected emission powered by radioactivity using their hydrodynamic and nucleosynthesis calculations. However, since the opacity in the r-process element-rich ejecta was poorly known, they have assumed that the

¹ National Astronomical Observatory of Japan, Mitaka, Tokyo, Japan; masaomi.tanaka@nao.ac.jp

² Department of Physics, Kyoto University, Kyoto, Japan; hotoke@tap.sphys.kyoto-u.ac.jp

opacity is similar to that of Fe-rich Type Ia SNe, i.e., $\kappa \sim 0.1 \text{ cm}^2 \text{ g}^{-1}$ (Pinto & Eastman 2000).

Recently, Kasen et al. (2013) and Barnes & Kasen (2013) evaluated the opacity of a few representative lanthanoid elements. They showed that the opacity of these elements are higher than that of Fe by a factor of about 100. They showed that the expected emission becomes fainter and longer than previously expected, as a result of the high opacity.

In this paper, we perform radiative transfer simulations for NS merger ejecta including *all* the r-process elements for the first time. For this purpose, we build a new line list for r-process elements from VALD database (Piskunov et al. 1995; Ryabchikova et al. 1997; Kupka et al. 1999, 2000), including about 100,000 bound-bound transitions. This strategy is complementary to that taken by Kasen et al. (2013) and Barnes & Kasen (2013), who constructed detailed models of a few lanthanoid elements.

We first describe the details of a newly-developed, three-dimensional (3D), time-dependent, and multi-frequency Monte Carlo (MC) radiative transfer code in Section 2. Models for the NS merger ejecta are presented in Section 3. We present results of radiative transfer simulations in Sections 4. We show that the opacity for the mixture of r-process elements is as high as $\kappa = 10 \text{ cm}^2 \text{ g}^{-1}$, which is consistent with the results by Kasen et al. (2013); Barnes & Kasen (2013). We also show that the spectral features are smeared out by bound-bound transitions of many different r-process elements. In Section 5, we demonstrate that the EM emission depends on the mass ratio of the binary NSs, and also on the equation of states (EOSs) adopted in the merger simulations. Based on these results, strategy for EM follow-up observations are discussed in Section 6. We also argue that the emission can be possibly detected in the afterglow of nearby short GRBs. Finally, we give conclusions in Section 7.

2. RADIATIVE TRANSFER CODE

2.1. Overview

We have developed a new 3D, time-dependent, multi-frequency radiative transfer code. The code can be applied both for NS merger ejecta and SN ejecta. For a given density structure and an abundance distribution, the code computes the time series of spectra in the UVOIR wavelength range. By integrating the spectra at a certain wavelength range with appropriate filter response curves, multi-color light curves are also computed. To solve radiative transfer, we adopt MC technique following Lucy (2005). The details of the code are presented in the subsequent sections. Here we briefly summarize the procedures of simulations.

After setting up the computational domain (Section 2.2), photon packets are created by taking into account the radioactive decay (^{56}Ni for SNe and many r-process nuclei for NS mergers, Section 2.3). For SNe, γ -ray transfer is solved under the gray approximation (Section 2.4). The absorbed γ -ray packets are converted into UVOIR packets (or so called *r*-packets by Lucy 2005). Transport of UVOIR packets is computed by taking into account the electron scattering, and free-free, bound-free and bound-bound transitions (Section 2.5).

By appropriately propagating the packets (Section 2.6), the temperature structure is determined based on the photon flux (Section 2.7). By using the new temperature structure, ionization and excitation conditions are computed under the assumption of local thermodynamic equilibrium (LTE, Section 2.8). Then, the UVOIR opacity is updated and MC transport is computed again. Since the temperature is not known at first, these iterative calculations are performed at each time step. Finally, escaping packets are counted, which naturally give the time series of UVOIR spectra (Section 2.9).

The validity of our code is tested by comparing our results with those with other numerical codes. First, a gray UVOIR transfer is tested for a simple model of Type Ia SN by Lucy (2005). Then, the multi-frequency transfer is tested with the standard W7 model for Type Ia SN (Nomoto et al. 1984). For both cases, we confirm a good agreement with the results with 3D MC gray transfer code by Lucy (2005), 3D MC multi-frequency codes by Kasen et al. (2006) and by Kromer & Sim (2009), and one-dimensional (1D) multi-frequency code by Blinnikov et al. (1998); Blinnikov & Sorokina (2000). Results of the test calculations are presented in Appendix A.

2.2. Setup of computational domain

A density structure and an abundance distribution are mapped into 3D Cartesian grid. We typically use 32^3 cells. Thanks to the nearly homologous expansion of SN ejecta and NS merger ejecta (each fluid element expands in the radial direction as $r = vt$, where t is the time after the explosion or after the merger), we use velocity as a spatial coordinate. The use of velocity coordinate has a great advantage since we treat a wide range of time, spanning about 2 orders of magnitude. For a typical NS merger model, a spatial resolution is $\Delta v \sim 2000 \text{ km s}^{-1}$ ($\Delta v \sim 1000 \text{ km s}^{-1}$ for a typical SN model). We do not consider any back reaction from radiation to hydrodynamics. Thus, the density in each cell is simply updated as $\rho \propto t^{-3}$.

For the time grid, we use a logarithmically-spaced time step. Simulations are performed typically from 0.1 days to 30 days with a time step of $\Delta \log(t/\text{day}) = 0.02$ for NS merger models (from 2 days to 50 days for SN models). For the frequency grid, we use a linearly-spaced grid in the wavelength, typically $\lambda = 100 - 25000 \text{ \AA}$ with $\Delta \lambda = 10 \text{ \AA}$. At the center of the optical wavelength ($\sim 6000 \text{ \AA}$), this wavelength resolution corresponds to the velocity resolution of $\Delta v \simeq 500 \text{ km s}^{-1}$.

2.3. Creation of packets

For MC radiative transfer, we use energy packets having equal energy (e.g., Lucy 2005). First, the total radioactive energy E_{rad} is divided into N packets, so that each packet has an equal comoving-frame energy $\epsilon_0 = E_{\text{rad}}/N$.

For the case of SNe, each packet is created as a γ -ray packet. According to the total energy release by ^{56}Ni decay (E_{Ni}) and ^{56}Co decay (E_{Co}), each packet is designated as that from ^{56}Ni or ^{56}Co ; a fraction $E_{\text{Ni}}/E_{\text{rad}}$ is a ^{56}Ni packet while $E_{\text{Co}}/E_{\text{rad}}$ is a ^{56}Co packet. If a packet is a ^{56}Ni packet, the decay time is assigned by $t_{\text{active}} = -t_{\text{Ni}} \ln z$, where t_{Ni} is the lifetime of ^{56}Ni . Hereafter, z is a random number from 0 to 1. Similarly, if a

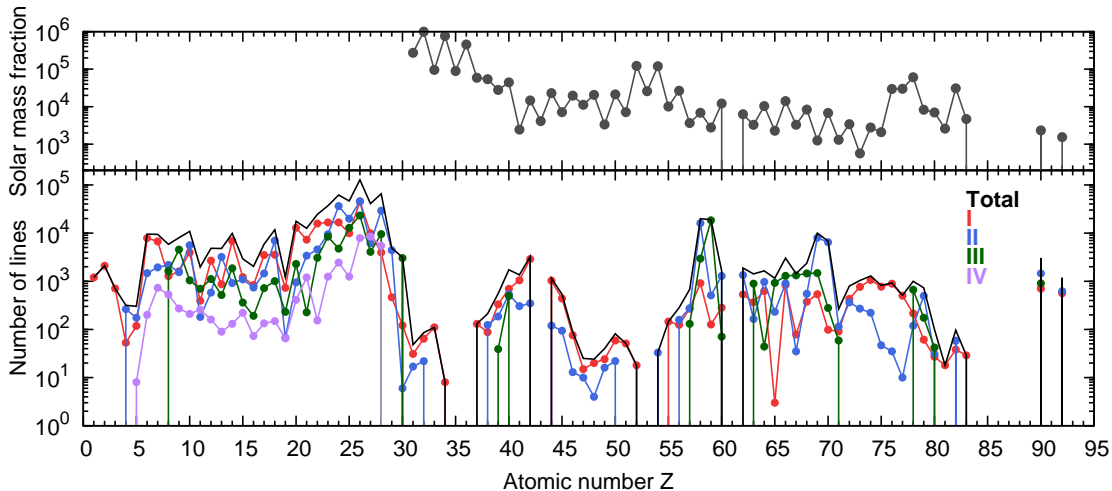


FIG. 1.— (*Upper*) Solar abundance r-process abundance ratio in mass fraction (Simmerer et al. 2004). The abundance is normalized with $X(\text{Ge}) = 10^6$. (*Lower*) The number of bound-bound transition data for different elements. Different colors show different ionization states, from neutral (I) to triply ionized (IV) ions. The atomic data at $Z \leq 30$ are taken from Kurucz & Bell (1995) while the data at $Z \geq 31$ are compiled using the VALD database (Piskunov et al. 1995; Ryabchikova et al. 1997; Kupka et al. 1999, 2000). It is shown that there is no data for triply ionized ions (IV, purple) at $Z \geq 31$.

packet is a ^{56}Co packet, $t_{\text{active}} = -t_{\text{Ni}} \ln z_1 - t_{\text{Co}} \ln z_2$, where t_{Co} is the lifetime of ^{56}Co (z_1 , and z_2 are independent random numbers from 0 to 1). These γ -ray packets are activated once the computation reaches at $t > t_{\text{active}}$. An isotropic direction in comoving frame is also assigned for each packet.

For the heating by many r-process radioactive nuclei in the NS merger ejecta, Metzger et al. (2010) showed the total radioactive power follows $t^{-1.2}$ (see also Korobkin et al. 2012). Thus, a time of activation of each packet is assigned as $t_{\text{active}} = t_{0,\text{decay}} z^{-5}$, so that it reproduces the energy release following $t^{-1.2}$. Here $t_{0,\text{decay}}$ is the beginning of the radioactive energy release. In this paper, we set $t_{0,\text{decay}} = 10^{-4}$ days, which is sufficiently earlier than the initial time of the simulations. When the computation reaches to $t > t_{\text{active}}$, UVOIR packets are created (instead of γ -ray packet for the case of SNe, see Section 3). Similar to the case of SNe, an isotropic direction in comoving frame is assigned. For the UVOIR packets, the initial co-moving wavelength is assigned by sampling emissivity j_λ (Section 2.6).

Both for the cases of SNe and NS mergers, when the time of the activation of a packet is earlier than the initial time of the simulation ($t_{\text{active}} < t_0$, where t_0 is the initial time of the simulation), the packet is created as a UVOIR packet at $t = t_0$. To take into account the energy loss by adiabatic expansion, the comoving-frame energy ϵ is reduced to $\epsilon = \epsilon_0(t_{\text{active}}/t_0)$ (Lucy 2005).

Note that the current code does not take into account the heating by the shock wave (see e.g., Kasen et al. 2006). Thus, the code cannot be applied for Type IIP SNe, where the shock heating is a dominant source of radiation at the plateau phase (up to ~ 100 days).

2.4. γ -ray transfer

For the case of SNe, γ -ray transfer is computed. We adopt the gray approximation with a mass absorption coefficient of $\kappa_\gamma = 0.027 \text{ cm}^2 \text{ g}^{-1}$, which is known to reproduce the results of multi-energy transport and the observed light curves of Type Ia SNe (Colgate et al. 1980;

Sutherland & Wheeler 1984; Maeda 2006). This is also confirmed by our test calculations (Appendix A). Once a γ -ray packet is absorbed, it is immediately converted to a UVOIR packet. For the case of NS mergers, the effect of γ -ray transport is taken into account by introducing a thermalization factor, and γ -ray transfer is not directly computed (see Section 3).

2.5. UVOIR transfer

Transfer of UVOIR packets is computed considering a wavelength-dependent opacity. As opacity sources, we consider the electron scattering, and free-free, bound-free, and bound-bound transitions. The wavelength-dependent opacity is evaluated in each cell after the temperature estimate in each time step. The bound-bound transition is the dominant source of opacity both for Type Ia SNe and NS mergers.

Electron scattering: By solving the Saha equations, the number density of free electrons (n_e) is computed in each cell. The absorption coefficient of electron scattering is evaluated as $\alpha^{\text{es}} = n_e \sigma_{\text{Th}}$, where σ_{Th} is the cross section of electron scattering (or Thomson scattering).

Free-free transition: Free-free absorption coefficient for an ion (i -th element and j -th ionization stage) is computed as in Rybicki & Lightman (1979), using common convention;

$$\alpha_{i,j}^{\text{ff}}(\lambda) = \frac{4e^6}{3m_e h c} \left(\frac{2\pi}{3km_e} \right)^{1/2} T^{-1/2} (j-1)^2 n_e n_{i,j} \nu^{-3} (1 - e^{-h\nu/kT}) \bar{g}_{\text{ff}}, \quad (1)$$

where T , $n_{i,j}$ are the electron temperature (which is assumed to be the same with radiation temperature, Section 2.7), and the number density of the ion. Here \bar{g}_{ff} is a velocity-averaged Gaunt factor, which is set to be unity in our code. The absorption coefficient is evaluated for all the ions included in the ejecta.

Bound-free transition: For the bound-free absorption coefficients, we adopt

$$\alpha_{i,j}^{\text{bf}}(\lambda) = n_{i,j} \sigma_{i,j}^{\text{bf}}, \quad (2)$$

where $\sigma_{i,j}^{\text{bf}}$ is the cross section of bound-free transition for an ion. For the cross section, we use analytic formulae by Verner et al. (1996), which is expressed by 7 parameters. They cover elements from H through Si, and S, Ar, Ca and Fe for all the ionization stages. The missing data are replaced with those of the closest elements.

Since there is no data for elements heavier than Fe, we simply use the cross section of Fe for all the heavier elements. This crude assumption does not affect our conclusions for the emission from NS mergers. The bound-free opacity can be dominant only at $\lambda \lesssim 1000 \text{ \AA}$, while a typical radiation temperature we treat is $T_R < 10,000 \text{ K}$. Thus, the bound-free opacity does not have a strong impact on the overall properties of the radiation.

Bound-bound transition: The bound-bound transition is treated using “the expansion opacity” introduced by Karp et al. (1977). We adopt the formula by Eastman & Pinto (1993);

$$\alpha_{\text{exp}}^{\text{bb}}(\lambda) = \frac{1}{ct} \sum_l \frac{\lambda_l}{\Delta\lambda} (1 - e^{-\tau_l}), \quad (3)$$

which is also adopted by Kasen et al. (2006). The summation is taken for all the lines within a wavelength interval of $\Delta\lambda$. Here, λ_l and τ_l are the wavelength and the Sobolev optical depth of a transition, respectively. In homologously expanding ejecta, the Sobolev optical depth can be written as

$$\tau_l = \frac{\pi e^2}{m_e c} \left(\frac{n_{i,j} \lambda_l t}{g_0} \right) g_l f_l \exp^{-E_l/kT}. \quad (4)$$

Here g_l , E_l , f_l are the statistical weight and the energy of the lower level of the transition, and the oscillator strength of the transition, respectively (g_0 is the statistical weight for the ground level).

For the properties of bound-bound transitions (λ_l , g_l , E_l , and f_l), the line list by Kurucz & Bell (1995, CD23) is adopted. This list includes about 500,000 lines, and has been widely used for radiative transfer of SNe (Kasen et al. 2006; Kromer & Sim 2009). In Appendix A, we demonstrate that this list gives reasonable light curves and spectra of Type Ia SNe.

For NS mergers, the dominant elements in the ejecta may be r-process elements (with $Z \geq 31$). For such heavy elements, Kurucz’s line list includes the data only for neutral or some singly ionized ions. Thus, we constructed a line list for elements heavier than Ga ($Z = 31$) using the VALD database (Piskunov et al. 1995; Ryabchikova et al. 1997; Kupka et al. 1999, 2000)³. Figure 1 shows the number of bound-bound transitions as a function of atomic number. Our list includes the data up to doubly ionized ions. In total, about 100,000 lines are added at $Z \geq 31$. The limitation of this line list is discussed in Appendix B.

We treat all the bound-bound transition as purely absorptive (see discussion by Nugent et al. 1997). As demonstrated by Kasen et al. (2006), this choice gives a reasonable spectral series and light curves for Type Ia SNe. We also confirmed this in our test calculations (see Appendix A).

³ <http://vald.astro.univie.ac.at/~vald/php/vald.php>

2.6. Treatment of events

In MC radiative transfer, propagation of packets is directly followed. To evaluate what kind of events packets experience, 3 distances are computed for each packet: (1) the distance to the scattering or absorption events l_1 , (2) the distance to the next cell l_2 , and (3) the distance that a packet can travel before the next time step l_3 . For the distance to the scattering or absorption events, we first set a threshold optical depth $\tau_{\text{th}} = -\ln z$. Then, by using the total absorption coefficient for UVOIR photons

$$\alpha^{\text{tot}}(\lambda) = \alpha^{\text{es}} + \sum_{i,j} \alpha_{i,j}^{\text{ff}}(\lambda) + \sum_{i,j} \alpha_{i,j}^{\text{bf}}(\lambda) + \alpha_{\text{exp}}^{\text{bb}}(\lambda), \quad (5)$$

the distance is computed from $l_1 = \tau_{\text{th}}/\alpha^{\text{tot}}(\lambda)$, so that it reproduces the attenuation following $\exp(-\tau)$. For the γ -ray transfer, $\alpha^{\text{tot}} = \kappa_{\gamma}\rho$.

Among the three distances, the event with the shortest distance occurs. When l_1 is the shortest, we judge if it is a scattering event or an absorption event. For the γ -ray transfer, it is always an absorption event. For the UVOIR transfer, only the electron scattering is a scattering event, so that an event is treated as scattering if $z < \alpha^{\text{es}}/\alpha^{\text{tot}}$. For the scattering event, the co-moving wavelength and energy of a packet are conserved. For the absorption event, the next co-moving wavelength is determined by sampling the emissivity (by Kirchoff’s law)

$$j_{\lambda} = \alpha^{\text{abs}}(\lambda) B_{\lambda}(T), \quad (6)$$

where α^{abs} is the total coefficient for absorptive events

$$\alpha^{\text{abs}}(\lambda) = \sum_{i,j} \alpha_{i,j}^{\text{ff}}(\lambda) + \sum_{i,j} \alpha_{i,j}^{\text{bf}}(\lambda) + \alpha_{\text{exp}}^{\text{bb}}(\lambda). \quad (7)$$

When l_2 is the shortest, the comparison among l_1 , l_2 , and l_3 is repeated again in the next cell. These procedures are repeated until l_3 becomes the shortest. When l_3 is the shortest, the position and direction of the packet are recorded, and the propagation of the next packet is considered. After computing the propagation of all the packets in a time step, the propagation in the next time step is computed.

2.7. Temperature determination

After the propagation of the packets, the temperature in each cell is evaluated by using the photon flux. In MC transfer, the photon intensity is evaluated (Lucy 2003) as

$$J_{\nu} d\nu = \frac{1}{4\pi\Delta t V} \sum_{\nu} \epsilon ds. \quad (8)$$

The temperature is estimated by approximating that the wavelength-integrated intensity $\langle J \rangle = \int J_{\nu} d\nu$ follows Stefan-Boltzmann law, i.e.,

$$\langle J \rangle = \frac{\sigma}{\pi} T_R^4. \quad (9)$$

This is the same assumption with the “simple” case of Kromer & Sim (2009). It is confirmed that this method gives reasonable results in Appendix A. We assume that the kinetic temperature of electron T_e is the same with the radiation temperature T_R . We simply denote them by T , i.e., $T = T_e = T_R$.

2.8. Ionization and excitation

For ionization, we assume LTE and solve the Saha equations for H through U simultaneously. We use NIST database⁴ for the atomic data, such as partition functions and ionization potentials. For the excitation, we assume Boltzmann distribution with the temperature T .

In the NS merger ejecta, radioactive decay produces fast β -decay electrons, fission products, and gamma-rays in the NS merger ejecta. Thus, possible deviation from LTE by these non-thermal ionization and excitation processes may be expected. In fact, non-thermal effect is known to be important for excitation of He lines in Type Ib SNe (Lucy 1991; Dessart et al. 2011; Hachinger et al. 2012). However, Kasen et al. (2013) estimated that the non-thermal excitation rate in a typical environment of the NS merger ejecta (blackbody temperature of 5000 K at $t = 1$ day) is only $\sim 10^{-8}$ of the radiative excitation rate by blackbody field. This implies that non-thermal processes do not affect ionization and excitation states significantly. Nevertheless, it must be noted that the deviation from LTE is expected to be larger at later epochs as the blackbody temperature decreases and the ejecta becomes more transparent.

2.9. Observations

Escaping γ -ray packets and UVOIR packets are counted. They naturally give a γ -ray light curve and a UVOIR light curve. Since each UVOIR packet has a wavelength, time series of spectra are also obtained. Multi-color light curves are computed by adopting the standard optical *UBVRI* filters (Bessell 1990) and NIR *JHK* filters (Persson et al. 1998) with the zero-magnitude flux by Bessell et al. (1998). AB magnitudes using Sloan Digital Sky Survey *ugriz* filters (Fukugita et al. 1996) and *JHK* filters are also computed.

3. MODELS AND SETUP

3.1. Ejecta Models

We adopt two kinds of models for NS merger ejecta (Table 1). The first sets are simple models with a power-law density structure, and the others are realistic models based on the results of merger simulations by Hotokezaka et al. (2013).

For simple cases, we use a model introduced by Metzger et al. (2010). The density structure follows $\rho \propto r^{-3}$ from $v = 0.05c - 0.2c$. The total ejecta mass is set to be $M_{\text{ej}} = 0.01M_{\odot}$. This model has a total kinetic energy of $E_{\text{K}} = 1.3 \times 10^{50}$ erg. We define the characteristic velocity of the ejecta by $v_{\text{ch}} = \sqrt{2E_{\text{K}}/M_{\text{ej}}}$. Then, the characteristic velocity of this model is $v_{\text{ch}} = 0.12c$. The ejecta include a mixture of r-process elements, i.e., Ga through U. For relative mass fractions, we assume the solar abundance ratios of r-process elements by Simmerer et al. (2004). Hereafter, we call this fiducial model “NSM-all”

To see the effect of element abundances to the opacity, we also test additional three models: (1) “NSM-dynamical”: a model only with $Z \geq 55$, which may be realized when the r-process nucleosynthesis is efficient in the dynamical ejecta, and the final element abundances

are dominantly determined by fission cycles. (2) “NSM-wind”: a model with $31 \leq Z \leq 54$. These relatively light elements can be abundant if the wind or outflow from a black hole torus, which can subsequently occur after the NS merger, dominates the ejecta (Wanajo & Janka 2012; Fernández & Metzger 2013). (3) “NSM-Fe”: a hypothetical model only with Fe. To see the effect to the opacity, the heating rate is kept the same in these models (Section 3.2).

The other sets of models are constructed from results of numerical simulations. Hotokezaka et al. (2013) performed extensive numerical-relativity simulations for various mass of neutron stars and EOSs. We map the density distribution of the ejecta (the material that has a higher expansion velocity than the escape velocity at the end of the simulations) into a two-dimensional, axisymmetric model. We adopt 4 models from their simulations (Table 1). The adopted EOSs are a “soft” EOS APR4 (Akmal et al. 1998) and a “stiff” EOS H4 (Glendenning & Moszkowski 1991; Lackey et al. 2006), which give the radius of 11.1 km and 13.6 km for a $1.35M_{\odot}$ neutron star (in gravitational mass), respectively. In this paper, we use terminology of “soft” for EOSs giving smaller radii of NSs. The gravitational masses of NSs are $1.2M_{\odot} + 1.5M_{\odot}$ and $1.3M_{\odot} + 1.4M_{\odot}$.⁵ See Hotokezaka et al. (2013) for more details.⁶

3.2. Setup

The major difference between SN ejecta and NS merger ejecta comes from the heating source. SN ejecta are dominantly heated by the decay of ^{56}Ni while NS merger ejecta are heated by the decay of many different radioactive r-process nuclei with different decay timescales. Metzger et al. (2010) showed that the energy release per unit mass is $\sim 3 \times 10^{15} (t/t_{0,\text{decay}})^{-1.2}$ erg $\text{s}^{-1} \text{g}^{-1}$, which does not depend strongly on the models (see also Korobkin et al. 2012). Thus, we assume that the total radioactive power is proportional to the total ejecta mass, and adopt

$$\dot{E}_{\text{decay}} = 6 \times 10^{46} \left(\frac{M_{\text{ej}}}{0.01M_{\odot}} \right) \left(\frac{t}{t_{0,\text{decay}}} \right)^{-1.2} \text{ erg s}^{-1}. \quad (10)$$

As introduced in Section 2.3, we set $t_{0,\text{decay}} = 10^{-4}$ days. As long as it is sufficiently earlier than the initial time of the simulations, this choice does not affect the light curve since most of the energy released at such an early stage is lost by adiabatic expansion.

From this total power, about 90% of the energy is released by β decay while the other 10% by fission (Metzger et al. 2010). For the β decay, neutrinos, electrons, and γ -rays carry about 25%, 25%, and 50% of the energy, respectively. The energy carried out by electrons and by fission products is likely to be deposited without significant escape, while that by neutrinos can escape almost entirely. Following the method by Metzger et al. (2010) and Korobkin et al. (2012), we introduce the efficiency of thermalization ϵ_{therm} for the β -decay energy.

⁵ In this paper, the mass ratio is defined as M_1/M_2 , where M_1 and M_2 are the mass of two NSs and $M_1 > M_2$.

⁶ The kinetic energy shown in Table 1 is somewhat different from that shown by Hotokezaka et al. (2013) because we smoothed the density structure of numerical results and remapped it into coarse grids.

⁴ <http://www.nist.gov/pml/data/asd.cfm>

TABLE 1
 SUMMARY OF MODELS

| Model | M_{ej} (M_{\odot}) | E_K (erg) | v_{ch} | Abundance ¹ |
|---------------|------------------------------------|----------------------|-----------------|------------------------|
| NSM-all | 1.0×10^{-2} | 1.3×10^{50} | 0.12c | $31 \leq Z \leq 92$ |
| NSM-dynamical | 1.0×10^{-2} | 1.3×10^{50} | 0.12c | $55 \leq Z \leq 92$ |
| NSM-wind | 1.0×10^{-2} | 1.3×10^{50} | 0.12c | $31 \leq Z \leq 54$ |
| NSM-Fe | 1.0×10^{-2} | 1.3×10^{50} | 0.12c | $Z = 26$ (only Fe) |
| APR4-1215 | 8.6×10^{-3} | 4.3×10^{50} | 0.24c | $31 \leq Z \leq 92$ |
| APR4-1314 | 8.1×10^{-3} | 3.6×10^{50} | 0.22c | $31 \leq Z \leq 92$ |
| H4-1215 | 3.5×10^{-3} | 1.4×10^{50} | 0.21c | $31 \leq Z \leq 92$ |
| H4-1314 | 7.0×10^{-4} | 1.9×10^{49} | 0.17c | $31 \leq Z \leq 92$ |

NOTE. — ¹ Solar abundance ratios (Simmerer et al. 2004) are assumed.

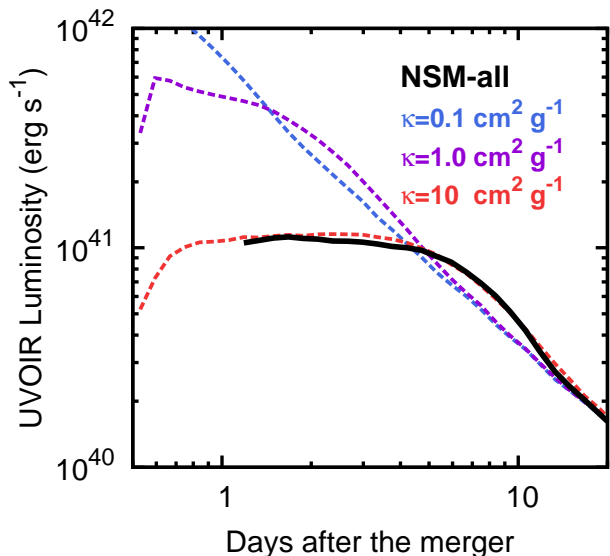


FIG. 2.— Bolometric light curve of model NSM-all (black, multi-frequency simulations). It is compared with the light curves for the same model but with the gray approximation of UVOIR transfer ($\kappa = 0.1, 1,$ and $10 \text{ cm}^2 \text{ g}^{-1}$ for blue, purple, and red lines, respectively). The result of multi-frequency transfer are most similar to that of gray transfer with $\kappa = 10 \text{ cm}^2 \text{ g}^{-1}$.

Then, the radiation energy can be written as

$$\dot{E}_{\text{rad}} = (0.1 + 0.9\epsilon_{\text{therm}})\dot{E}_{\text{decay}}. \quad (11)$$

The thermalization efficiency must be in the range of $\epsilon_{\text{therm}} = 0.25 - 0.75$, depending on the efficiency of γ -ray energy deposition. By adopting $\epsilon_{\text{therm}} = 0.5$, we assume that the energy E_{rad} is immediately deposited without transportation (i.e., we neglect γ -ray transfer, and UVOIR packets are created directly).

4. RESULTS

Figure 2 shows the computed bolometric light curve for the fiducial model NSM-all (black line). It is compared with the light curves for the same model but with the gray approximation of the UVOIR transfer. The blue, purple, and red lines show the cases with gray mass absorption coefficients of $\kappa = 0.1, 1.0,$ and $10 \text{ cm}^2 \text{ g}^{-1}$, respectively. The result of multi-frequency transfer closely follows the light curve with the gray opacity of $\kappa = 10 \text{ cm}^2 \text{ g}^{-1}$. This indicates that r-process

element-rich NS merger ejecta are more opaque than previously assumed ($\kappa \simeq 0.1 \text{ cm}^2 \text{ g}^{-1}$, e.g., Li & Paczyński 1998; Metzger et al. 2010), by a factor of about 100. As a result, the bolometric light curve becomes fainter, and the time scale becomes longer.⁷ This is consistent with the findings by Kasen et al. (2013) and Barnes & Kasen (2013).

Figure 3 shows the mass absorption coefficient as a function of wavelength at $t = 3$ days in model NSM-all at $v = 0.1c$. The mass absorption coefficient is as high as $1\text{-}100 \text{ cm}^2 \text{ g}^{-1}$ in the optical wavelengths. The resulting Planck mean mass absorption coefficient is about $\kappa = 10 \text{ cm}^2 \text{ g}^{-1}$ (Figure A4). This is the reason why the bolometric light curve of multi-frequency transfer most closely follows that with gray opacity of $\kappa = 10 \text{ cm}^2 \text{ g}^{-1}$ in Figure 2.

The high opacity in r-process element-rich ejecta is also confirmed by the comparison with other simple models. Figure 4 shows the comparison of the bolometric light curve among models NSM-all, NSM-dynamical, NSM-wind, and NSM-Fe. Compared with NSM-Fe, the other models show the fainter light curves. This indicates that the elements heavier than Fe contribute to the high opacity. The opacity in model NSM-Fe is also shown in Figure 3. It is nicely shown that opacity in NSM-all is higher than that in NSM-Fe by a factor of about 100 at the center of optical wavelengths ($\sim 5000 \text{ \AA}$).

As inferred from Figure 4, NSM-dynamical ($55 \leq Z \leq 92$) has a higher opacity than that of NSM-wind ($31 \leq Z \leq 54$). This is because lanthanoid elements ($57 \leq Z \leq 71$) have the largest contribution to the bound-bound opacity, as demonstrated by Kasen et al. (2013). Note that, however, even with the elements at $31 \leq Z \leq 54$, the opacity is higher than that of Fe.

Figure 5 shows the multi-color light curves of model NSM-all. In general, the emission from NS merger ejecta is red because of (1) a lower temperature than SNe and (2) a higher optical opacity than in SNe. In particular, the optical light curves in the blue wavelengths drop dramatically in the first 5 days. The light curves in

⁷ We show the results of our multi-frequency transfer simulations at $t \gtrsim 1$ day. Because of the lack of bound-bound transition data for triply ionized ions in our line list (Figure 1), the opacity at earlier epoch is not correctly evaluated. We hereafter show the results when the temperature at the characteristic velocity is below $10,000 \text{ K}$, when the dominant ionization states are no more triply ionized ions. Detailed discussion is presented in Appendix B.

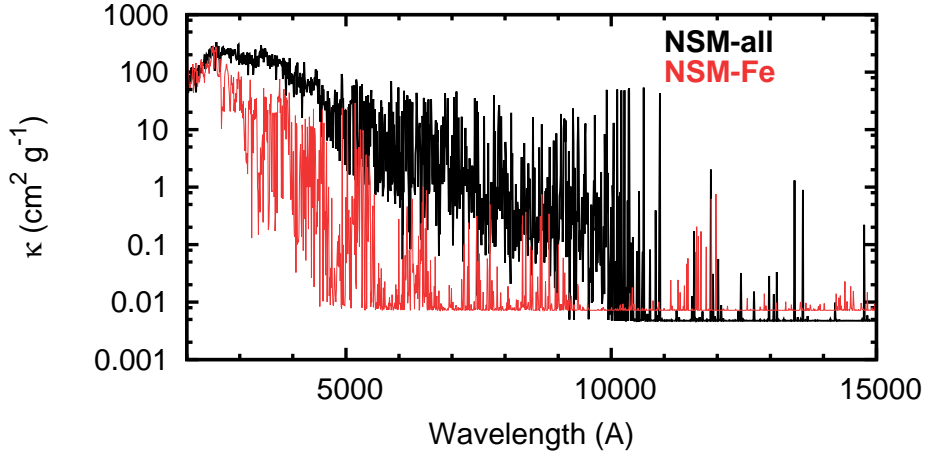


FIG. 3.— Mass absorption coefficient κ at $v = 0.1c$ in model NSM-all and NSM-Fe as a function of wavelength ($t = 3$ days after the merger). In r-process element-rich ejecta, the opacity is higher than Fe-rich ejecta by factor of about 100 around the center of optical wavelength (~ 5000 Å).

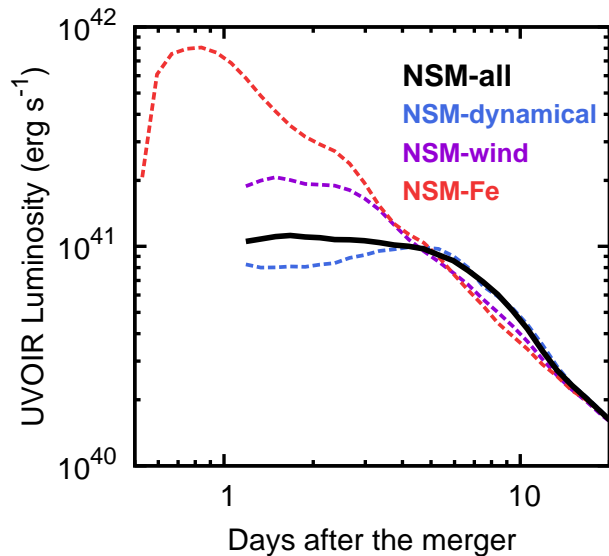


FIG. 4.— Bolometric light curves for simple models with different element abundances: NSM-all ($31 \leq Z \leq 92$), NSM-dynamical ($55 \leq Z \leq 92$), NSM-wind ($31 \leq Z \leq 54$), and NSM-Fe (only Fe).

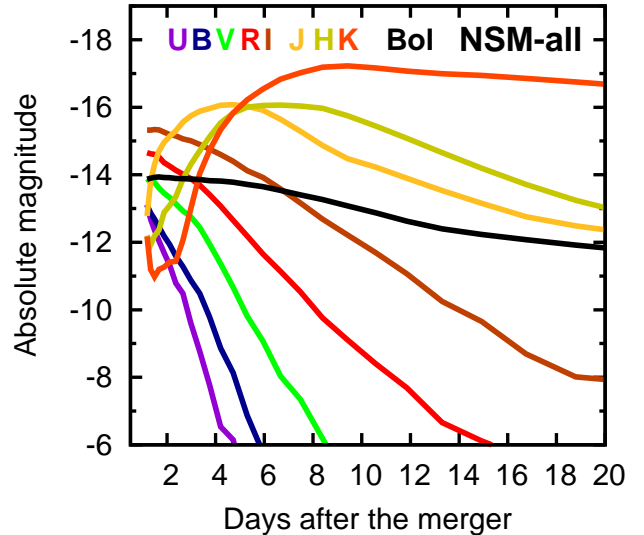


FIG. 5.— Multi-color light curves of model NSM-all (in Vega magnitude). Light curves in redder bands are brighter and slower.

the redder band evolves more slowly. This trend is also consistent with the results by Kasen et al. (2013) and Barnes & Kasen (2013).

Since our simulations include all the r-process elements, spectral features are of interest. Since the simulations by Kasen et al. (2013) and Barnes & Kasen (2013) include only a few lanthanoid elements, they do not discuss the detailed spectral features. Figure 6 shows the spectra of model NSM-all at $t = 1.5, 5.0$ and 10.0 days after the merger. Our spectra are almost featureless at all the epochs. This is because of the overlap of many bound-bound transitions of different r-process elements. As a result, compared with the results by Kasen et al. (2013) and Barnes & Kasen (2013), the spectral features are more smeared out.

Note that we could identify possible broad absorption features around $1.4 \mu\text{m}$ (in the spectrum at $t = 5$ days)

and around $1.2 \mu\text{m}$ and $1.5 \mu\text{m}$ ($t = 10$ days). In our line list, these bumps are mostly made by a cluster of the transitions of Y I, Y II, and Lu I. However, we are cautious about such identifications because the bound-bound transitions in the VALD database are not likely to be complete in the NIR wavelengths even for neutral and singly ionized ions. In fact, Kasen et al. (2013) showed that the opacity of Ce from the VALD database drops in the NIR wavelengths, compared with the opacity based on their atomic models. Although we cannot exclude a possibility that a cluster of bound-bound transitions of some ions can make a clear absorption line in NS mergers, our current simulations do not provide prediction for such features.

5. DEPENDENCE ON THE EOS AND MASS RATIO

Figure 7 shows the bolometric light curves of realistic models. The luminosity is averaged over all solid an-

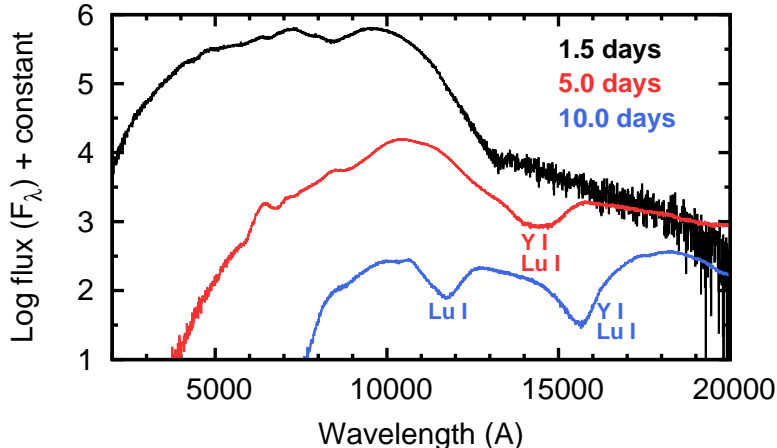


FIG. 6.— UVOIR spectra of model NSM-all at $t = 1.5, 5.0,$ and 10.0 days after the merger. The spectra are almost featureless. At NIR wavelengths, there are possible absorption troughs, which result from Y I, Y II, and Lu I in our simulations. However, the features could be result from the incompleteness of the line list in the NIR wavelengths.

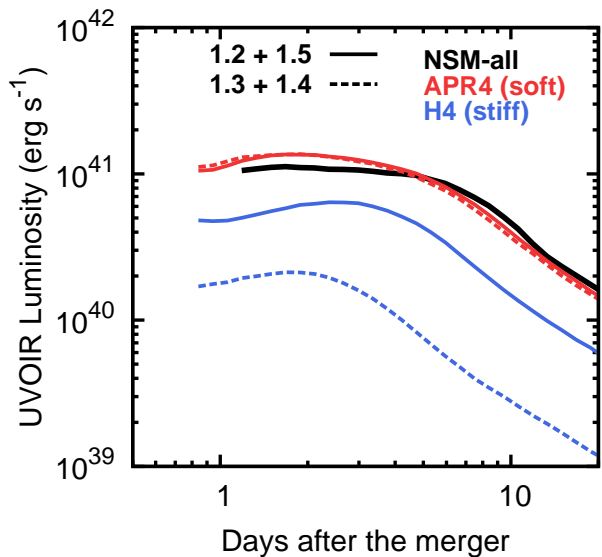


FIG. 7.— Bolometric light curves for realistic models (Table 1). The luminosity is averaged over all solid angles. The expected emission of models with a soft EOS APR4 (red) is brighter than that with a stiff EOS H4 (blue). For the soft EOS APR4, the light curve does not depend on the mass ratio, while for a stiff EOS H4, a higher mass ratio ($1.2M_{\odot} + 1.5M_{\odot}$, solid line) results in a large ejecta mass, and thus, brighter emission than a lower mass ratio ($1.3M_{\odot} + 1.4M_{\odot}$, dashed line).

gles. Since the angle dependence is within a factor of 2 (brighter in the polar direction, see Roberts et al. 2011), we focus only on the averaged luminosity.

The models with the soft EOS APR4 (red) is brighter than the models with the stiff EOS H4 (blue). This is interpreted as follows. When the total radioactive power is proportional to the ejecta mass (Equation 10), the peak luminosity is expected to scale as $L \propto M_{\text{ej}}^{1/2} v_{\text{ch}}^{1/2}$ (Li & Paczyński 1998). We confirmed that the peak luminosity of our models roughly follows this relation (an effective opacity is $\kappa \sim 10 \text{ cm}^2 \text{ g}^{-1}$ irrespective of models). For a soft EOS (i.e., a smaller radius of a NS), the mass ejection occurs at a more compact orbit and

shock heating is efficient. As a result, the mass of the ejecta is higher for softer EOSs (see Table 1, and also Hotokezaka et al. 2013; Bauswein et al. 2013). Therefore, the NS merger with the soft EOS APR4 is brighter. Note that the light curve of the fiducial model NSM-all (black) is similar to that of model APR4-1215 and APR4-1314 because these models have a similar mass and a characteristic velocity (Table 1).

For the soft EOS APR4, the brightness does not depend strongly on the mass ratio of the binary NSs (red solid and dashed lines in Figure 7). This is because for a soft EOS, such as APR4, the mass ejection by shock heating is efficient. By contrast, for the stiff EOS H4, the mass ejection occurs primarily by tidal effects (the effect of shock heating is weak, Hotokezaka et al. 2013). Thus, the mass ejection is more efficient for a higher mass ratio. As a result, model H4-1215 (mass ratio of 1.25) is brighter than model H4-1314 (mass ratio of 1.08).

These results open a new window to study the nature of the NS merger and EOSs. By adding the information of EM radiation to the analysis of GW signals, we may be able to pin down the masses of two NSs and/or stiffness of the EOSs more accurately. Note that, in the current simulations, the heating rate per mass is fixed. To fully understand the connection between the initial condition of the NS merger and expected emission, detailed nucleosynthesis calculations are necessary.

6. IMPLICATIONS FOR OBSERVATIONS

6.1. Follow-up Observations of EM Counterparts

In this section, we discuss the detectability of UVOIR emission from NS merger ejecta. Figure 8 shows expected observed light curves for a NS merger event at 200 Mpc. Model NSM-all (black) and 4 realistic models (red and blue) are shown. Note that all the magnitudes in Figure 8 are given in AB magnitude for the ease of comparison with different survey projects. Horizontal lines show 5σ limiting magnitudes for different sizes of telescopes with 10 min exposure time.

After the detection of GW signal, EM follow up observations should discover a new transient object from a $\sim 10\text{-}100 \text{ deg}^2$ area. Thus, the use of wide-field tele-

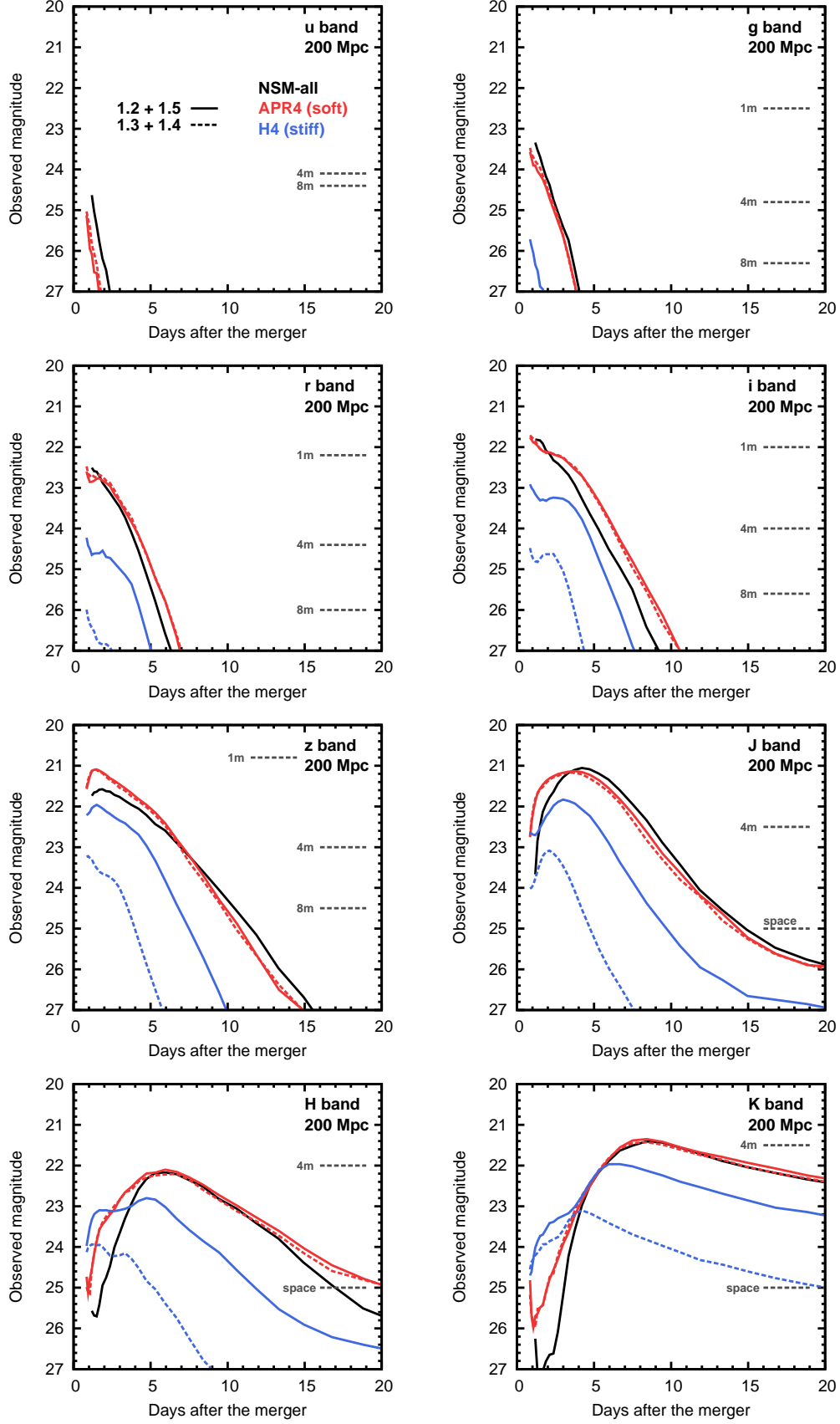


FIG. 8.— Expected observed *ugrizJHK*-band light curves (in AB magnitude) for model NSM-all and 4 realistic models. The distance to the NS merger event is set to be 200 Mpc. *K* correction is taken into account with $z = 0.05$. Horizontal lines show typical limiting magnitudes for wide-field telescopes (5σ with 10 min exposure). For optical wavelengths (*ugriz* bands), “1 m”, “4 m”, and “8 m” limits are taken or deduced from those of PTF (Law et al. 2009), CFHT/Megacam, and Subaru/HSC (Miyazaki et al. 2006), respectively. For NIR wavelengths (*JHK* bands), “4 m” and “space” limits are taken or deduced from those of Vista/VIRCAM and the planned limits of WFIRST (Green et al. 2012) and WISH (Yamada et al. 2012), respectively.

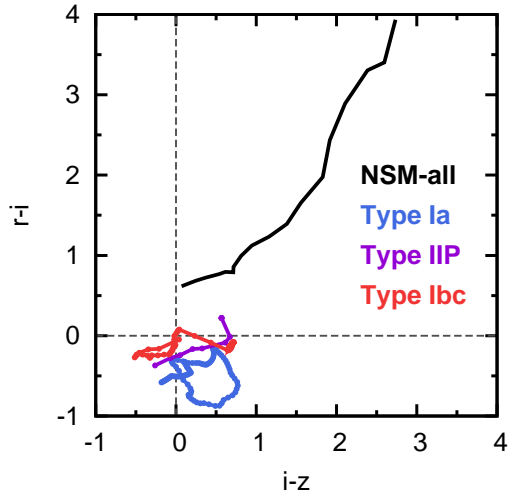


FIG. 9.— Color-color diagram for the NS merger (black) compared with Type Ia (blue), Type IIP (purple), and Type Ic (red) SNe. The emission from NS merger ejecta is much redder than that of SNe. For SNe, we use the spectral templates by Nugent et al. (2002). All the magnitudes are in AB magnitude and in the rest frame (i.e., no K correction).

scope/camera is a natural choice (e.g., Kelley et al. 2012; Nissanke et al. 2013). For optical wavelengths, there are several projects using 1 m-class telescopes that can cover $\gtrsim 4$ deg² area, such as Palomar transient factory (PTF, Law et al. 2009; Rau et al. 2009), La Silla-QUEST Variability Survey (Hadjiyska et al. 2012), and Catalina Real-Time Transient Survey (Drake et al. 2009). In Figure 8, we show the limiting magnitudes deduced from Law et al. (2009). Because of the red color, the detection in blue wavelengths (ug bands) seems difficult. Even for the bright cases, deep observations with > 10 min exposure in red wavelengths (i or z bands) are needed. The faint models are far below the limit of 1m-class telescopes.

For larger optical telescopes, the field of view tends to be smaller. Among 4m-class telescopes, Canada-France-Hawaii Telescope (CFHT)/Megacam and the Blanco 4m telescope/DECAM for the Dark Energy Survey⁸ have 3.6 deg² and 4.0 deg² field of view, respectively. In Figure 8, we show the limiting magnitudes from CFHT/Megacam⁹. The bright models (red and black lines) are above the limits at the first 5-10 days. Similar to 1m-class telescopes, observations in redder wavelengths are more efficient. The faintest model (model H4-1314, blue dashed line) is still below the limit of 4m-class telescopes with 10 min exposure.

To cover all the possibilities, we need 8m-class telescopes. Among such large telescopes, only Subaru/Hyper Suprime Cam (HSC, Miyazaki et al. 2006) and Large Synoptic Survey Telescope (LSST, Ivezić et al. 2008; LSST Science Collaborations et al. 2009) have a wide field of view (1.77 deg² and 9.6 deg², respectively). We show the expected limit with Subaru/HSC. In red optical wavelengths (i or z bands), 8m-class telescope can detect

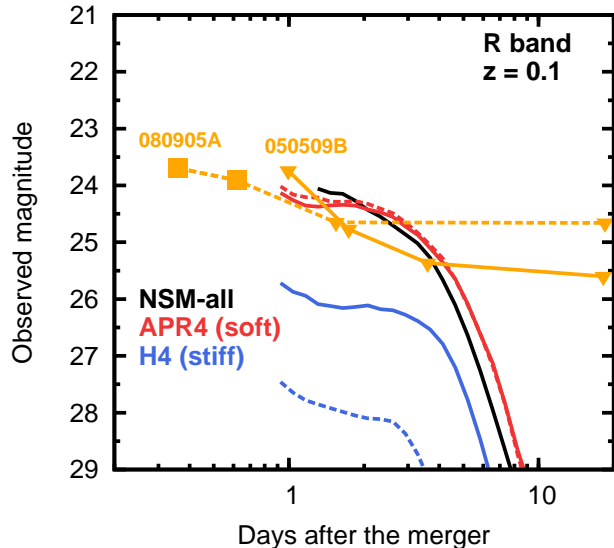


FIG. 10.— Observed R -band light curves of the models at $z = 0.1$ (in Vega magnitude, with K correction) compared with the deep detection or upper limits of short GRB afterglow (GRBs 050509B and 080905A). For the afterglow data, we use R -band magnitude corrected and shifted to $z = 0.1$ scale (Kann et al. 2011). The squares show the detections while the triangles show upper limits. Deep observations of short GRB afterglow are about to make constraints on the emission powered by radioactive energy.

even the faintest case.

In Figure 9, we show a $r-i$ vs $i-z$ color-color diagram for model NSM-all compared with that of Type Ia, IIP, and Ibc SNe (Nugent et al. 2002). As clearly seen, the NS merger is significantly redder than SNe. Thus, confusion with SNe will not be problematic.

Because of the extremely red color, follow up observations in NIR wavelengths are also useful. In NIR wavelengths, however, a field of view is usually smaller than in optical. We plot the limit of 4.1m VISTA telescope/VIRCAM (~ 0.6 deg² Dalton et al. 2006)¹⁰. In J band, ground-based observations with 4m-class telescopes will be able to detect a bright event in NIR wavelengths.

Observations from space seem a more promising strategy (see also Barnes & Kasen 2013). The Wide-Field Infrared Survey Telescope (WFIRST, Green et al. 2012) and Wide-field Imaging Surveyor for High-redshift (WISH, Yamada et al. 2012) are planned to perform wide-field survey in NIR wavelengths. Their planned field of views are 0.375 deg² and 0.28 deg², respectively. Their typical limiting magnitude is ~ 25 mag with ~ 10 min observations. They will be able to detect even the faintest case (Figure 8).

We conclude that extensive follow-up observations with wide-field 4m- and 8m-class telescopes in optical and wide-field space telescopes in NIR are crucial to detect the EM counterpart of GW sources. In optical, i or z -band observations are the most efficient. The observations should be performed within about 5 days (for optical) and 10 days (for NIR) from the detection of GWs.

6.2. Search for Emission in Short GRB Afterglow

⁸ <https://www.darkenergysurvey.org>

⁹ <http://www.cfht.hawaii.edu/Instruments/Imaging/Megacam/general.html>

¹⁰ <http://www.eso.org/sci/facilities/paranal/instruments/vircam/>

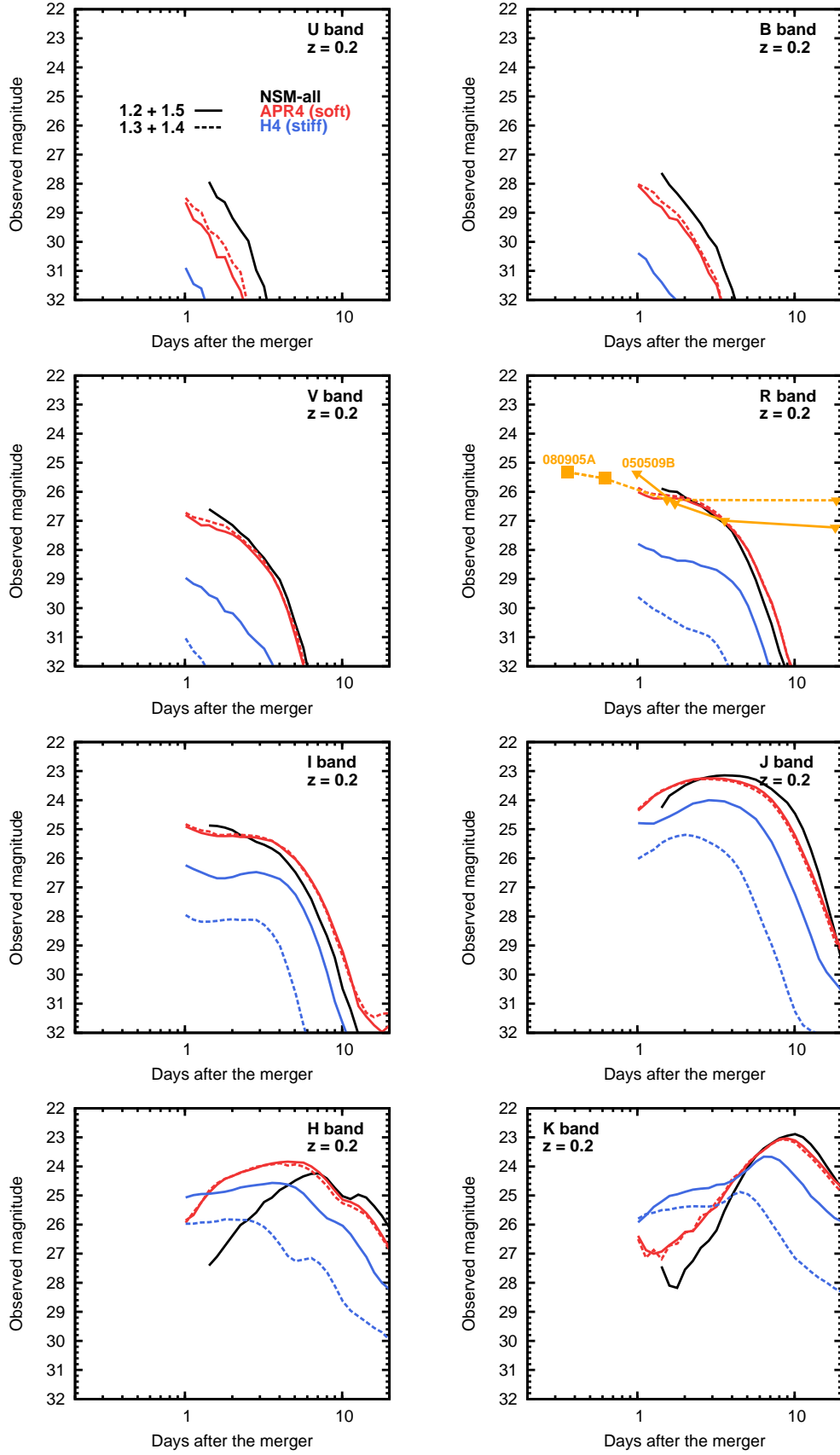


FIG. 11.— Expected observed $UBVRJJK$ -band light curves (in Vega magnitude) of the NS merger at $z = 0.2$. Deep follow-up observations of short GRB afterglows will be able to detect a radioactive “bump”. K correction is taken into account for the models. In the R -band light curve, deepest observational limits for short GRBs so far (GRBs 050509B and 080905A, Kann et al. 2011) are plotted. The squares show the detections while the triangles show upper limits. Note that the original data by Kann et al. (2011) are corrected and shifted to $z = 0.1$ scale, and we correct only the distance (to $z = 0.2$) in this plot.

Although the emission from a NS merger by radioactive decay energy has not been detected, we show that it may be possible to detect the emission as a “bump” in the afterglow of short GRBs when the afterglow is faint enough. If such a bump is detected, it proves that (1) nucleosynthesis involving radioactive nuclei takes place in the NS merger ejecta and (2) such emission can actually be used to identify the GW sources. Although extensive search has been performed for relatively nearby short GRBs, no such an extra component has been detected (e.g., Fox et al. 2005; Hjorth et al. 2005b,a; Perley et al. 2009; Rowlinson et al. 2010; Kocevski et al. 2010).

Figure 10 shows the model light curves at $z = 0.1$. The models (black, red and blue lines) are compared with the deepest observations of short GRBs so far (GRBs 050509B and GRB 080905A) compiled by Kann et al. (2011). The data are corrected and shifted to $z = 0.1$ scale by Kann et al. (2011) with an appropriate K -correction. The squares show the detections while the triangles show upper limits. For original data, see Gehrels et al. (2005); Hjorth et al. (2005a); Castro-Tirado et al. (2005); Bersier et al. (2005); Bloom et al. (2006) for GRB 050509B and Rowlinson et al. (2010) for GRB 080905A. Before the correction of redshift, the deepest limits for GRB 050509B ($z=0.225$) are ~ 26.5 mag (Bersier et al. 2005), and those for 080905A ($z=0.1218$) are ~ 25.0 mag (Rowlinson et al. 2010).

The upper limits are, in fact, very close to the expected light curves with $M_{\text{ej}} \sim 0.01M_{\odot}$. We do *not* argue that the current deep limits already exclude such an ejecta mass because we made an assumption that the heating rate is simply proportional to the total ejecta mass, and there is still an uncertainty in the absolute brightness. However, it is encouraging that the deepest observations actually about to make constraints on the emission by radioactive energy.

Figure 11 shows the expected light curves at $z = 0.2$ (in Vega magnitude, with appropriate K corrections). For short GRBs at $z = 0.2$, R -band observations down to 27 (31) mag at $\lesssim 3$ days from the burst may be able to detect the emission powered by radioactivity if the bright (faint) model is the case. As already discussed, observations in redder wavelengths are more efficient. In I band, observations down to 26 (29) mag may detect the bright (faint) case. In NIR wavelengths, the “bump” can be as bright as 23-25 mag (in Vega magnitude). When the afterglow is faint enough not to overshadow these emission, we may be able to make constraints on the efficiency of mass ejection and nucleosynthesis in the NS merger ejecta ¹¹.

7. CONCLUSIONS

We perform radiative transfer simulations for NS merger ejecta powered by radioactive energy of r-process nuclei. This is the first simulation including all the r-process elements from Ga to U. We show that the opacity in the NS merger ejecta is higher than previously

expected by a factor of ~ 100 due to many bound-bound transitions of r-process elements. A typical mass absorption coefficient is $\kappa \sim 10 \text{ cm}^2 \text{ g}^{-1}$ ($\kappa \sim 0.1 \text{ cm}^2 \text{ g}^{-1}$ for Fe-rich Type Ia SNe). This is consistent with the recent results by Kasen et al. (2013) and Barnes & Kasen (2013), who computed opacity of a few lanthanoid elements with detailed models of these ions. As a result of high opacity, the emission powered by radioactive energy is fainter and longer than previously thought.

Spectroscopic features are important to identify a new source as a NS merger event. Because of the high expansion velocity ($v \sim 0.1c$), a single absorption line from r-process elements cannot be resolved. In addition, by including all the r-process elements in the simulations, spectroscopic features are almost totally smeared out. We may recognize the NS merger event by their featureless spectra with a very red color.

By using the results of numerical simulations for NS merger by Hotokezaka et al. (2013), we demonstrate that NS merger with a higher mass ratio is brighter. When a softer EOS is applied in the merger simulations, the emission is also brighter. This opens a new window to study the nature of the NS merger events and EOSs by EM observations (see also Bauswein et al. 2013).

At 200 Mpc, an expected horizon for GW detection, the expected brightness is $g = 23\text{-}27$ mag, $r = 23 - 26$ mag, $i = 22 - 25$ mag, $z = 21 - 23$ mag in optical, and 21-24 mag in NIR JHK bands (in AB magnitude). The emission is brighter and lasts longer in redder wavelengths. Therefore, extensive follow-up observations with wide-field 4m- and 8m-class telescopes in optical (such as CFHT/Megacam, Blanco 4m/DECam, Subaru/HSC and LSST) and wide-field space telescopes in NIR (e.g., WFIRST and WISH) are crucial to detect the EM counterpart of GW sources. In optical wavelengths, observations in the reddest bands (i or z bands) are the most efficient. The observations should be performed within about 5-10 days from the detection of GWs.

We show that the emission powered by radioactive energy can be possibly detected by deep follow-up observations of short GRB afterglow when the afterglow is faint enough. The current deepest limits for nearby short GRBs are already very close to the expected brightness. When our bright (faint) model is the case, observations down to $R = 27$ (31) mag, $I = 26$ (29) mag, or 24 (26) mag in NIR JHK bands (in Vega magnitude) for short GRBs at $z = 0.2$ will be able to detect the “bump”. If such emission is detected, it provides evidence that (1) nucleosynthesis involving radioactive nuclei takes place in the NS merger ejecta and (2) such emission can actually be used to identify the GW sources.

The authors thank Yuichiro Sekiguchi, Masaru Shibata, Kenta Kiuchi, Keiichi Maeda, and Koutarou Kyutoku for fruitful discussion that launched this work. We also thank Sergei Blinnikov, Dan Kasen, Markus Kromer, Leon Lucy, Stuart Sim, and Elena Sorokina for providing their results of radiative transfer simulations, and Ken Nomoto for providing W7 model. MT thanks Akimasa Kataoka, Shinya Wanajo, and Kunito Ioka for valuable discussion. We have made extensive use of NIST database for atomic data, and VALD database (Piskunov et al. 1995; Ryabchikova et al. 1997;

¹¹ After submission of this paper, possible sign of radioactive emission was reported for short GRB 130603B at $z = 0.36$ (Berger et al. 2013; Tanvir et al. 2013). The H -band magnitude is about 25-26 AB mag at $t \simeq 7$ days (in the rest frame). This brightness prefers to our bright models (NSM-all, APR4-1215, and APR4-1314) rather than the faint models (H4-1215 and H4-1314).

Kupka et al. 1999, 2000) for line lists. Atomic data compiled in the DREAM data base (Biémont et al. 1999) were extracted via VALD. A large part of numerical simulations presented in this paper were carried out with Cray XC30 at Center for Computational Astrophysics, National Astronomical Observatory of Japan. This re-

search has been supported by the Grant-in-Aid for Scientific Research of the Japan Society for the Promotion of Science (JSPS, 24740117) and Grant-in-Aid for Scientific Research on Innovative Areas of the Ministry of Education, Culture, Sports, Science and Technology (MEXT, 25103515).

REFERENCES

- Abadie, J., et al. 2010a, *Classical and Quantum Gravity*, 27, 173001
 —. 2010b, *Nuclear Instruments and Methods in Physics Research A*, 624, 223
- Accadia, T., et al. 2011, *Classical and Quantum Gravity*, 28, 114002
- Akmal, A., Pandharipande, V. R., & Ravenhall, D. G. 1998, *Phys. Rev. C*, 58, 1804
- Barnes, J., & Kasen, D. 2013, arXiv:1303.5787
- Bauswein, A., Goriely, S., & Janka, H.-T. 2013, arXiv:1302.6530
- Berger, E., Fong, W., & Chornock, R. 2013, arXiv:1306.3960
- Bersier, D., Fruchter, A., Rhoads, J., Levan, A., & Tanvir, N. 2005, *GRB Coordinates Network*, 3521, 1
- Bessell, M. S. 1990, *PASP*, 102, 1181
- Bessell, M. S., Castelli, F., & Plez, B. 1998, *A&A*, 333, 231
- Biémont, E., Palmeri, P., & Quinet, P. 1999, *Ap&SS*, 269, 635
- Blinnikov, S. I., Eastman, R., Bartunov, O. S., Popolitov, V. A., & Woosley, S. E. 1998, *ApJ*, 496, 454
- Blinnikov, S. I., & Sorokina, E. I. 2000, *A&A*, 356, L30
- Bloom, J. S., et al. 2006, *ApJ*, 638, 354
- Castro-Tirado, A. J., et al. 2005, *A&A*, 439, L15
- Colgate, S. A., Petschek, A. G., & Kriese, J. T. 1980, *ApJ*, 237, L81
- Coward, D. M., et al. 2012, *MNRAS*, 425, 2668
- Dalton, G. B., et al. 2006, in *Society of Photo-Optical Instrumentation Engineers (SPIE) Conference Series*, Vol. 6269, *Society of Photo-Optical Instrumentation Engineers (SPIE) Conference Series*
- Dessart, L., Hillier, D. J., Livne, E., Yoon, S.-C., Woosley, S., Waldman, R., & Langer, N. 2011, *MNRAS*, 414, 2985
- Drake, A. J., et al. 2009, *ApJ*, 696, 870
- Duez, M. D. 2010, *Classical and Quantum Gravity*, 27, 114002
- Eastman, R. G., & Pinto, P. A. 1993, *ApJ*, 412, 731
- Eichler, D., Livio, M., Piran, T., & Schramm, D. N. 1989, *Nature*, 340, 126
- Fernández, R., & Metzger, B. D. 2013, arXiv:1304.6720
- Fox, D. B., et al. 2005, *Nature*, 437, 845
- Freiburghaus, C., Rosswog, S., & Thielemann, F.-K. 1999, *ApJ*, 525, L121
- Fukugita, M., Ichikawa, T., Gunn, J. E., Doi, M., Shimasaku, K., & Schneider, D. P. 1996, *AJ*, 111, 1748
- Gehrels, N., et al. 2005, *Nature*, 437, 851
- Glendenning, N. K., & Moszkowski, S. A. 1991, *Physical Review Letters*, 67, 2414
- Goriely, S., Bauswein, A., & Janka, H.-T. 2011, *ApJ*, 738, L32
- Green, J., et al. 2012, arXiv:1208.4012
- Hachinger, S., Mazzali, P. A., Taubenberger, S., Hillebrandt, W., Nomoto, K., & Sauer, D. N. 2012, *MNRAS*, 422, 70
- Hadjiyska, E., et al. 2012, in *IAU Symposium*, Vol. 285, *IAU Symposium*, ed. E. Griffin, R. Hanisch, & R. Seaman, 324–326
- Hjorth, J., et al. 2005a, *ApJ*, 630, L117
 —. 2005b, *Nature*, 437, 859
- Hotokezaka, K., Kiuchi, K., Kyutoku, K., Okawa, H., Sekiguchi, Y.-i., Shibata, M., & Taniguchi, K. 2013, *Phys. Rev. D*, 87, 024001
- Hsiao, E. Y., Conley, A., Howell, D. A., Sullivan, M., Pritchett, C. J., Carlberg, R. G., Nugent, P. E., & Phillips, M. M. 2007, *ApJ*, 663, 1187
- Ivezic, Z., et al. 2008, arXiv:0805.2366
- Kann, D. A., et al. 2011, *ApJ*, 734, 96
- Karp, A. H., Lasher, G., Chan, K. L., & Salpeter, E. E. 1977, *ApJ*, 214, 161
- Kasen, D., Badnell, N. R., & Barnes, J. 2013, arXiv:1303.5788
- Kasen, D., Thomas, R. C., & Nugent, P. 2006, *ApJ*, 651, 366
- Kelley, L. Z., Mandel, I., & Ramirez-Ruiz, E. 2012, arXiv:1209.3027
- Kocevski, D., et al. 2010, *MNRAS*, 404, 963
- Kochanek, C. S., & Piran, T. 1993, *ApJ*, 417, L17
- Korobkin, O., Rosswog, S., Arcones, A., & Winteler, C. 2012, *MNRAS*, 426, 1940
- Kromer, M., & Sim, S. A. 2009, *MNRAS*, 398, 1809
- Kulkarni, S. R. 2005, arXiv:astro-ph/0510256
- Kupka, F., Piskunov, N., Ryabchikova, T. A., Stempels, H. C., & Weiss, W. W. 1999, *A&AS*, 138, 119
- Kupka, F. G., Ryabchikova, T. A., Piskunov, N. E., Stempels, H. C., & Weiss, W. W. 2000, *Baltic Astronomy*, 9, 590
- Kuroda, K., & LCGT Collaboration. 2010, *Classical and Quantum Gravity*, 27, 084004
- Kurucz, R. 1993, *Atomic data for opacity calculations*. Kurucz CD-ROM No. 1. Cambridge, Mass.: Smithsonian Astrophysical Observatory, 1993., 1
- Kurucz, R., & Bell, B. 1995, *Atomic Line Data* (R.L. Kurucz and B. Bell) Kurucz CD-ROM No. 23. Cambridge, Mass.: Smithsonian Astrophysical Observatory, 1995., 23
- Kurucz, R. L. 2006, in *EAS Publications Series*, Vol. 18, *EAS Publications Series*, ed. P. Stee, 129–155
- Lackey, B. D., Nayyar, M., & Owen, B. J. 2006, *Phys. Rev. D*, 73, 024021
- Lattimer, J. M., & Schramm, D. N. 1974, *ApJ*, 192, L145
 —. 1976, *ApJ*, 210, 549
- Law, N. M., et al. 2009, *PASP*, 121, 1395
- Lee, W. H., & Ramirez-Ruiz, E. 2007, *New Journal of Physics*, 9, 17
- Li, L.-X., & Paczyński, B. 1998, *ApJ*, 507, L59
- LIGO Scientific Collaboration et al. 2013, arXiv:1304.0670
 —. 2012, *A&A*, 539, A124
- LSST Science Collaborations et al. 2009, arXiv:0912.0201
- Lucy, L. B. 1991, *ApJ*, 383, 308
 —. 2003, *A&A*, 403, 261
 —. 2005, *A&A*, 429, 19
- Maeda, K. 2006, *ApJ*, 644, 385
- Mazzali, P. A., Röpke, F. K., Benetti, S., & Hillebrandt, W. 2007, *Science*, 315, 825
- Mazzali, P. A., Sauer, D. N., Pastorello, A., Benetti, S., & Hillebrandt, W. 2008, *MNRAS*, 386, 1897
- Metzger, B. D., & Berger, E. 2012, *ApJ*, 746, 48
- Metzger, B. D., et al. 2010, *MNRAS*, 406, 2650
- Miyazaki, S., et al. 2006, in *Society of Photo-Optical Instrumentation Engineers (SPIE) Conference Series*, Vol. 6269, *Society of Photo-Optical Instrumentation Engineers (SPIE) Conference Series*
- Nissanke, S., Kasliwal, M., & Georgieva, A. 2013, *ApJ*, 767, 124
- Nomoto, K., Thielemann, F.-K., & Yokoi, K. 1984, *ApJ*, 286, 644
- Nugent, P., Baron, E., Branch, D., Fisher, A., & Hauschildt, P. H. 1997, *ApJ*, 485, 812
- Nugent, P., Kim, A., & Perlmutter, S. 2002, *PASP*, 114, 803
- Perley, D. A., et al. 2009, *ApJ*, 696, 1871
- Persson, S. E., Murphy, D. C., Krzeminski, W., Roth, M., & Rieke, M. J. 1998, *AJ*, 116, 2475
- Pinto, P. A., & Eastman, R. G. 2000, *ApJ*, 530, 757
- Piran, T., Nakar, E., & Rosswog, S. 2013, *MNRAS*, 430, 2121
- Piskunov, N. E., Kupka, F., Ryabchikova, T. A., Weiss, W. W., & Jeffery, C. S. 1995, *A&AS*, 112, 525
- Rau, A., et al. 2009, *PASP*, 121, 1334
- Roberts, L. F., Kasen, D., Lee, W. H., & Ramirez-Ruiz, E. 2011, *ApJ*, 736, L21
- Rosswog, S. 2005, *ApJ*, 634, 1202
 —. 2013, *Royal Society of London Philosophical Transactions Series A*, 371, 20272
- Rosswog, S., Liebendörfer, M., Thielemann, F.-K., Davies, M. B., Benz, W., & Piran, T. 1999, *A&A*, 341, 499
- Rosswog, S., Piran, T., & Nakar, E. 2013, *MNRAS*, 430, 2585
- Rowlinson, A., et al. 2010, *MNRAS*, 408, 383
- Ryabchikova, T. A., Piskunov, N. E., Kupka, F., & Weiss, W. W. 1997, *Baltic Astronomy*, 6, 244
- Rybicki, G. B., & Lightman, A. P. 1979, *Radiative processes in astrophysics* (New York, Wiley-Interscience)
- Sim, S. A. 2007, *MNRAS*, 375, 154
- Sim, S. A., Kromer, M., Röpke, F. K., Sorokina, E. I., Blinnikov, S. I., Kasen, D., & Hillebrandt, W. 2010, in *Astronomical Society of the Pacific Conference Series*, Vol. 429, *Numerical Modeling of Space Plasma Flows*, *Astronom-2009*, ed. N. V. Pogorelov, E. Audit, & G. P. Zank, 148
- Simmerer, J., Sneden, C., Cowan, J. J., Collier, J., Woolf, V. M., & Lawler, J. E. 2004, *ApJ*, 617, 1091
- Stehle, M., Mazzali, P. A., Benetti, S., & Hillebrandt, W. 2005, *MNRAS*, 360, 1231
- Sutherland, P. G., & Wheeler, J. C. 1984, *ApJ*, 280, 282
- Tanaka, M., Mazzali, P. A., Stanishev, V., Maurer, I., Kerzendorf, W. E., & Nomoto, K. 2011, *MNRAS*, 410, 1725
- Tanvir, N. R., Levan, A. J., Fruchter, A. S., Hjorth, J., Wiersema, K., Tunnicliffe, R., & de Ugarte Postigo, A. 2013, arXiv:1306.4971
- Verner, D. A., Ferland, G. J., Korista, K. T., & Yakovlev, D. G. 1996, *ApJ*, 465, 487
- Wanajo, S., & Janka, H.-T. 2012, *ApJ*, 746, 180

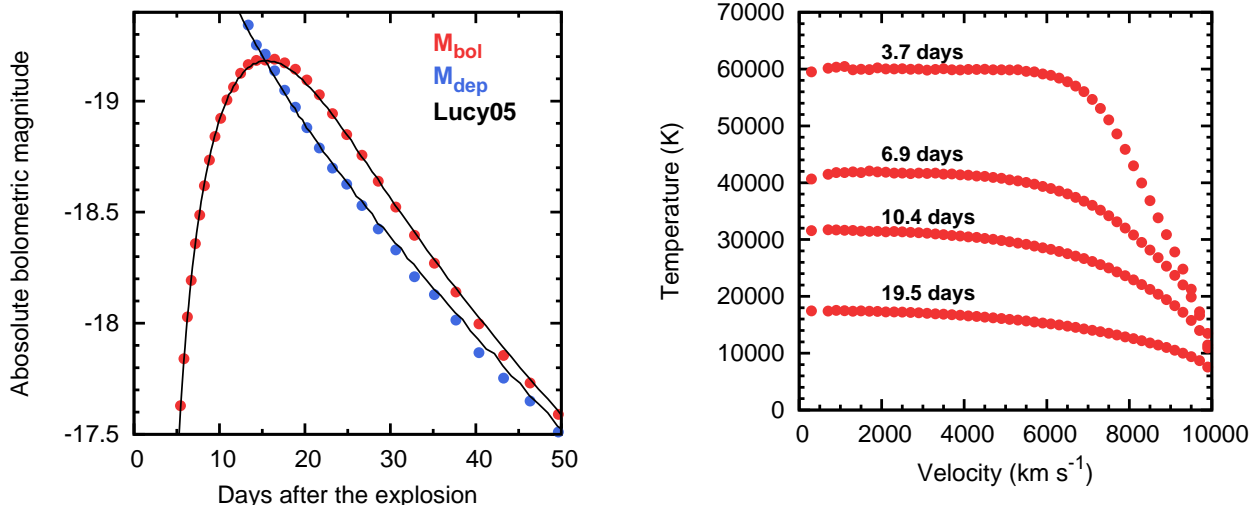


FIG. A1.— Test calculations with the simple Type Ia SN model by Lucy (2005) under gray approximation for UVOIR transfer. (*Left*) The bolometric luminosity (red) and deposited luminosity (blue) in absolute magnitude calculated with the new code. The solid lines show the corresponding results by Lucy (2005). (*Right*) Temperature structure as a function of velocity for different epochs.

Yamada, T., et al. 2012, in Society of Photo-Optical Instrumentation Engineers (SPIE) Conference Series, Vol. 8442, Society of Photo-Optical Instrumentation Engineers (SPIE) Conference Series

APPENDIX

APPENDIX A. TEST CALCULATIONS

A.1. Gray transfer

First we apply our new code for a simple Type Ia SN model introduced by Lucy (2005). The model has a uniform density distribution up to the maximum ejecta velocity of $10,000 \text{ km s}^{-1}$. The total ejecta mass is $1.39 M_{\odot}$. The model includes $0.65 M_{\odot}$ of ^{56}Ni . The distribution of ^{56}Ni is assumed to be constant at $M_r < 0.5 M_{\odot}$, while it drops linearly to zero at $M_r = 0.75 M_{\odot}$.

UVOIR transfer is performed under the gray approximation with $\kappa = 0.1 \text{ cm}^2 \text{ g}^{-1}$. The major difference between our code and that by Lucy (2005) is the γ -ray transfer. Lucy (2005) solves multi-energy γ -ray transport by taking into account Compton scattering and photoelectric absorption while our code adopt the gray approximation. We use an effective mass absorption coefficient of $\kappa = 0.027 \text{ cm}^2 \text{ g}^{-1}$, which is known to reproduce the results of multi-energy transport and the observed light curves of Type Ia SNe (Colgate et al. 1980; Sutherland & Wheeler 1984; Maeda 2006).

Our calculations (dots) and those by Lucy (2005, lines) show fairly good agreement (left panel of Figure A1). This indicates that our MC radiation solver works properly. Although we do not require a temperature structure for this calculation, Kasen et al. (2006) showed the temperature structure calculated with their 3D MC code. The temperature computed by our code (right panel of Figure A1) shows an excellent match with that by Kasen et al. (2006). It indicates that the temperature estimate in our code also works reasonably (Section 2.7).

A.2. Multi-frequency transfer

Next we apply our code for W7 model of Type Ia SN (Nomoto et al. 1984) with multi-frequency UVOIR transfer. This model has been used to test multi-frequency radiative transfer codes for SN ejecta. The model has a stratified abundance distribution; stable Fe-group layer ($M_r \lesssim 0.2 M_{\odot}$), ^{56}Ni layer ($M_r \simeq 0.2 - 0.8 M_{\odot}$, the total mass of ^{56}Ni is about $0.6 M_{\odot}$), Si and S-rich intermediate-mass element layer ($M_r \simeq 0.8 - 1.1 M_{\odot}$), and O-rich layer ($M_r \gtrsim 1.1 M_{\odot}$) from the center to the surface. Such a stratified distribution is also supported from observations (see e.g., Stehle et al. 2005; Mazzali et al. 2007, 2008; Tanaka et al. 2011).

Figure A2 shows comparisons of the bolometric and monochromatic light curves for W7 with different numerical codes. Models are also compared with the template light curves of Type Ia SN by Hsiao et al. (2007, gray dots). The red lines show our calculations. The blue lines show the results with the 3D MC code (SEDONA) by Kasen et al. (2006). This code adopts a big line list (including about 4×10^7 lines) by Kurucz (1993). The black and gray lines show the results with the 3D MC code (ARTIS) by Sim (2007) and Kromer & Sim (2009). The black line (“detailed”) shows the calculations with detailed ionization treatment by taking into account non-LTE effects and with a big bound-bound line list (including about 8×10^6 lines by Kurucz 2006). The gray line (“simple”) shows the calculations under LTE assumption with a moderate line list by Kurucz & Bell (1995), which our code also adopts. Thus, their simple case is more similar to our code. The green lines show the results with the 1D radiation hydrodynamic code

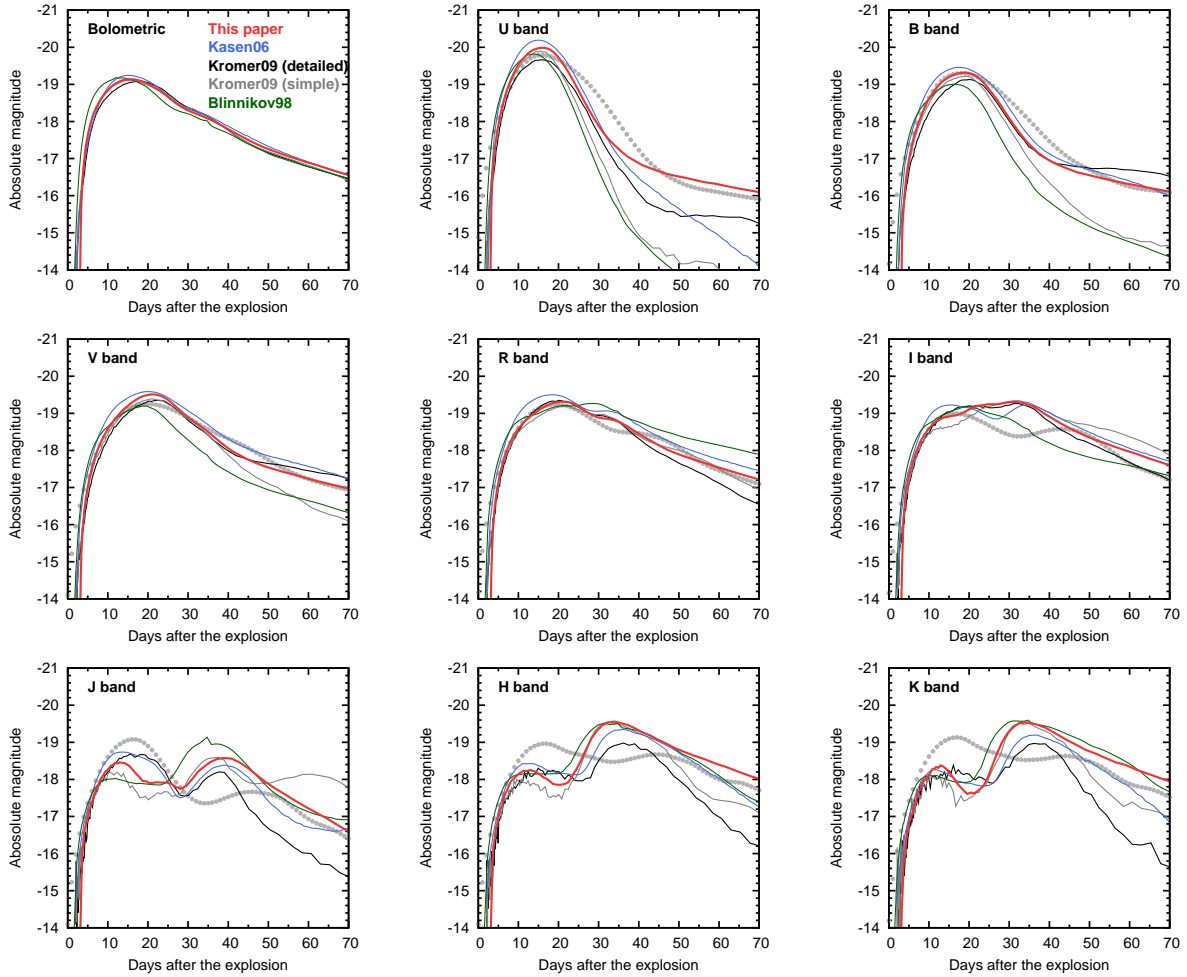


FIG. A2.— Comparison of light curves for W7 model with different numerical codes (lines): 3D MC codes by Kasen et al. (2006, blue), Kromer & Sim (2009, black and gray), and ours (red), and 1D radiation hydrodynamic code by Blinnikov et al. (1998, green). They are also compared with the template light curves of Type Ia SN by Hsiao et al. (2007, gray dots). For the template light curve, the rise time in B band is assumed to be 18 days.

by Blinnikov et al. (1998) Blinnikov & Sorokina (2000).

Given the complexity of the problem, the overall agreement among different codes is reasonable. The agreement in the bolometric luminosity is almost perfect. Generally, the agreement is better in optical wavelengths than in NIR wavelengths. The U -band light curves starts to differ at > 30 days after the explosion. Our code provides the best match with the observations at later epochs. The computed B , V , and R -band light curves agree with each other quite well, and they are also consistent with observations. The computed I -band light curves also agree among different codes, but they cannot reproduce a clear two peaks seen in the observations. This may be related to the treatment (absorptive or scattering) of the Ca II IR triplet line (Kasen et al. 2006). All the computed J , H , and K -band light curves show the two peaks, which are roughly consistent with the observations. With a closer look, computed light curves tend to show a fainter first peak and a brighter second peak than the observations. Kromer & Sim (2009) demonstrated the number of bound-bound transitions included in the simulation mostly affects the NIR light curves (black and gray lines in Figure A2). It is encouraging that with a bigger line list, the first (second) peak becomes brighter (fainter), which is closer to the observations. See also Sim et al. (2010) for a similar comparison and discussion.

Figure A3 shows the computed optical spectra at different epochs compared with the template spectra (Hsiao et al. 2007) in the corresponding phase. This also shows a reasonable agreement. As expected from the comparison of the light curves (Figure A2), the agreement of the overall color is not perfect at some epochs. Nevertheless, the strong absorption lines, such as those of O I, Si II, S II, Ca II, and Fe II, are produced at the right positions in the simulated spectra. This indicates that our code reasonably computes ionization states and opacity.

From these comparisons, we conclude that our new code works for multi-frequency UVOIR transfer with the Type Ia SN model. Simulations for NS merger ejecta are different from those for Type Ia SNe mostly in that the NS merger ejecta consist of heavier elements. However, we can consistently use the same Saha equation solver and the same format of the line list. Therefore, the simulations for NS merger do not require any computational technique that is not used in the simulation for Type Ia SNe.

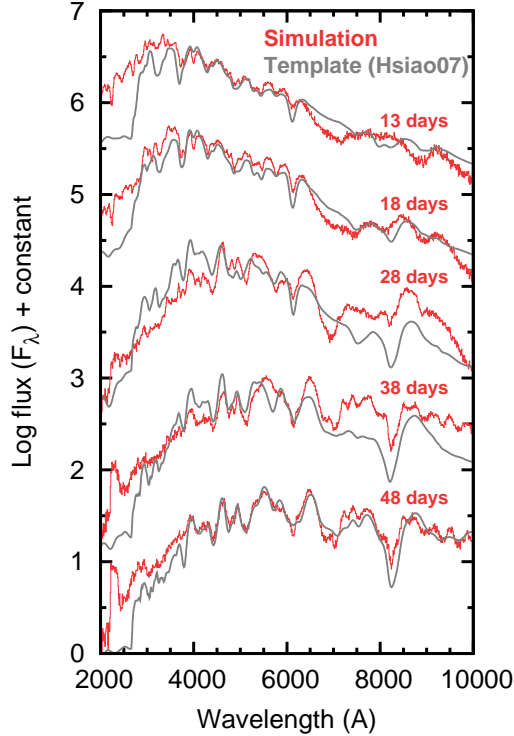


FIG. A3.— Computed time series of optical spectra for W7 model (red) compared with the spectral template of Type Ia SN by Hsiao et al. (2007, gray). The epoch shown in the panel is the time after the explosion. Observational template at the corresponding epoch are overplotted assuming the rise time in B band to be 18 days. The flux is arbitrarily scaled.

APPENDIX B. LIMITATION OF OUR LINE LIST

In the figures in the main text, we show our results of multi-frequency transfer for NS mergers only at $t \gtrsim 1$ day. Here we show the whole range of our results and discuss the limitation of our line list. The upper panel of Figure A4 shows the whole range of the computed bolometric light curve for model NSM-all. As clearly seen, the luminosity at $t < 1$ day is extremely high, reaching $\sim 5 \times 10^{43}$ erg s $^{-1}$. The lower panel of Figure A4 shows the Planck-mean mass absorption coefficient at $v = 0.1c$ in model NSM-all. The opacity at $t < 1$ day is extremely low, starting from $\sim 2 \times 10^{-2}$ cm 2 g $^{-1}$, which is found to be dominated by the electron scattering.

The reason of this low opacity is the incompleteness of our line list. As shown in Figure 1, our line list does not include the bound-bound data of triply ionized ions for the heavy elements with $Z \geq 31$. However, the ejecta are dominated by triply ionized ions at $t < 1$ day. Figure A5 shows the ionization fractions for different elements in the ejecta. At $t = 0.7$ day, triply ionized ions (purple) are dominated over the lower ionization states. As a result, the bound-bound opacity at such early epochs cannot be evaluated correctly.

This situation changes at later epochs. When the temperature is lower than 10,000 K (blue line in Figure A4), the dominant ionization states are no more triply ionized ions. The lower panel of Figure A5 shows the ionization at $t = 4$ day. At this epoch, the ejecta are dominated by singly and doubly ionized ions. Therefore, we use only the results at the epochs when the temperature at $v = v_{\text{ch}}$ is below 10,000 K.

One concern is a possible effect of the very low opacity to the later epoch. However, as shown in Figure 2, the results of the multi-frequency transfer at $t > 1$ day closely follow the light curve with the gray transfer with $\kappa = 10$ cm 2 g $^{-1}$. This is consistent with the expectation from the Planck-mean opacity at $t > 1$ day in multi-frequency transfer (Figure A4). Thus, we conclude that the light curve at $t > 1$ day is not significantly affected by the low opacity at earlier epochs.

It is noted that, for the case of SNe, we do not encounter a similar problem primarily because the bound-bound data include triply ionized ions at $Z \leq 30$. In addition to this, there is an important difference in the ionization states in the SN ejecta and NS merger ejecta. Since the mean atomic mass is heavier in the NS merger ejecta, the number density of ions is smaller in the NS merger ejecta than in Type Ia SN ejecta. As a result, the number density of free electrons is also smaller in the NS merger ejecta. Thus, for a given temperature and a density, the ionization states in the NS merger ejecta are higher than those in Type Ia SN ejecta. Therefore, simulations for NS mergers more easily encounter the incompleteness in the bound-bound data of highly-ionized ions.

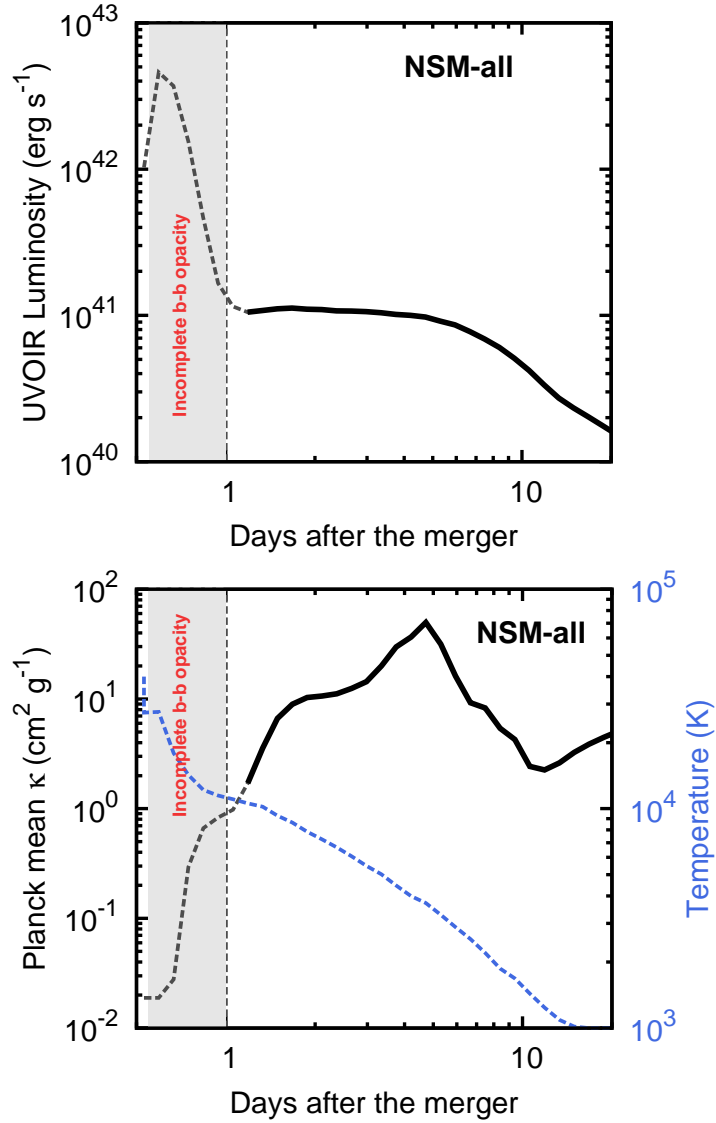


FIG. A4.— (*Upper*) Bolometric light curve of model NSM-all. (*Lower*) Planck-mean opacity (black) and temperature (blue) at $v = 0.1c$. Gray hatched area shows the epoch when the temperature at $v = 0.1c$ is $T \gtrsim 10000$ K. At such early epochs, our line list is not applicable, and the opacity is extremely low. This low opacity makes an unphysical early peak in the light curve.

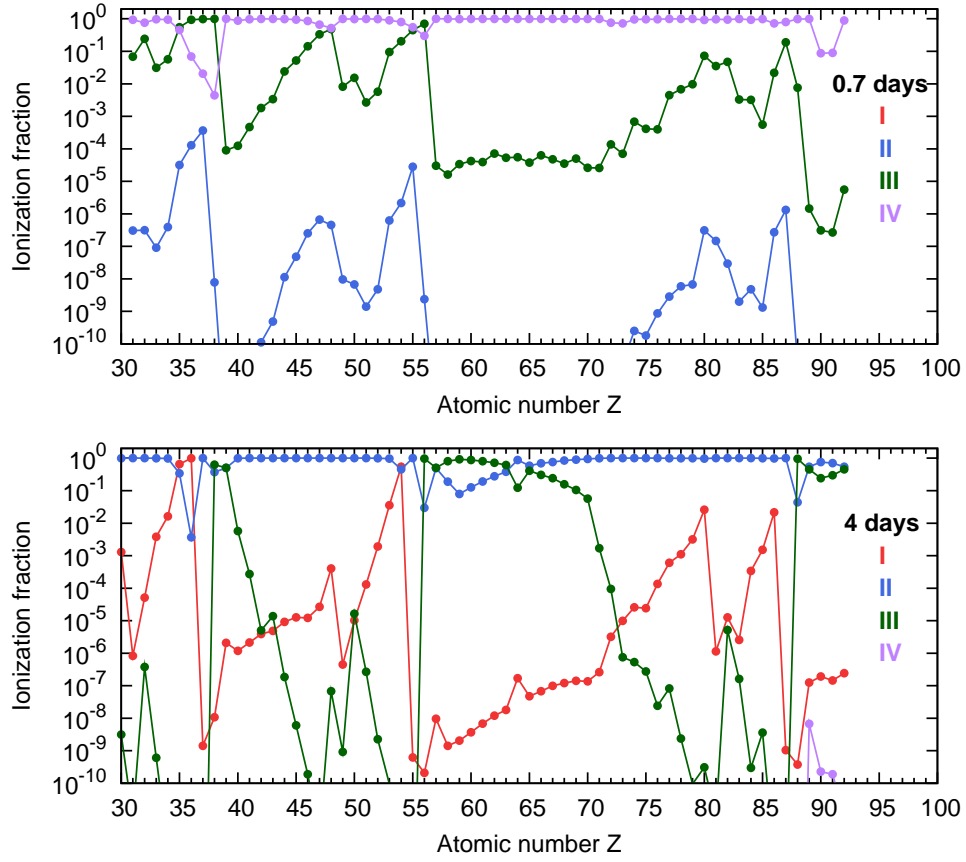


FIG. A5.— Ionization states for different elements at $v = 0.1c$ (in model NS-all) at $t = 0.7$ days (upper) and 4 days (lower) after the merger. It is shown that at $t = 0.7$ days, most of elements are triply ionized, which our line list does not cover (see Figure 1). At $t = 4$ days, dominant ionization states are singly or doubly ionized ions.